Chemical pressure and charge-density waves in rare-earth tritellurides

E. DiMasi and M. C. Aronson
Harrison M. Randall Laboratory of Physics, University of Michigan, Ann Arbor, Michigan 48109-1120

J. F. Mansfield
Electron Microbeam Analysis Laboratory, University of Michigan, Ann Arbor, Michigan 48109-2143

B. Foran and S. Lee
Willard H. Dow Laboratory of Chemistry, University of Michigan, Ann Arbor, Michigan 48109-1055
(Received 27 June 1995)

We report the results of transmission electron microscopy on the layered rare-earth tritellurides $R\mathrm{Te}_3$ (R=La,Sm,Gd,Tb,Dy,Ho,Er,Tm). Through electron diffraction we have identified superlattice reflections indicating the presence of incommensurate distortions, consistent with sinusoidal atomic displacements in the square Te sheets. The superlattice wave vector corresponds to the maximal Fermi-surface nesting wave vector determined from extended Hückel tight-binding band calculations. The charge-density wave (CDW) is stable under the volume decrease obtained by substituting the heavier rare earths, and the distortion wave vector scales with the lattice parameters across the rare-earth series. Our results indicate that the rare-earth tritellurides host small-amplitude Fermi surface driven distortions. We find no evidence for substantial deviation from sinusoidal atomic displacements, in contrast to the large commensurate distortions and ordered vacancy structures found in other rare-earth polychalcogenide phases. Our observations establish the rare-earth polychalcogenides as a family of CDW hosts in which a variety of structural distortions occur with variation of chalcogen type and stoichiometry, despite a very simple but universal chalcogen sheet band structure.

I. INTRODUCTION

Recognition of the charge-density wave (CDW) as an instability dependent on the Fermi surface has allowed the interpretation of the structural distortions of many families of materials. Examples include the transition-metal di- and trichalcogenides,[1,2] molybdenum and tungsten oxides such as the low-dimensional blue and purple bronzes,[3] organic charge transfer salts,[4] and elemental Se and Te.[5] The Fermi surfaces of these materials have nesting sheets that determine the wave vector of the distortion, and so the period of the superlattice is fixed by the geometry of the band structure at the Fermi level. However, different configurations of atomic displacements are possible within the superlattice determined by the nesting wave vector. The different modulated structures reflect subtle differences in high-temperature electronic structure and in general are not equally energetically favorable, as the energy gained in the distortion depends on the dispersion of the bands near the Fermi surface. While the geometry of the high-temperature Fermi surface fixes the superlattice wave vector, more detailed microscopic information is required to understand what makes a particular arrangement of atomic displacements most favorable at reduced temperature.[6]

Due in part to the variety of structural distortions observed in different families of materials, two somewhat different, though ultimately equivalent, approaches to the CDW have developed. Early formulations of the CDW instability considered sinusoidal atomic displacements, combined with an electron-phonon coupling, which together produce a gap at the Fermi surface.[7] The stability of this spatially uniform distortion is derived from the lowered energy of occupied states near the Fermi level. As the gap may appear over only part of the Fermi surface, the distorted system may still be metallic. Temperature dependence is implicit in this description of the CDW, as occupation of states with increased energy above the gap ultimately makes the distortion unfavorable. Alternatively, the CDW can be described as a Jahn-Teller distortion in which large displacements reduce atomic coordination.[8,9] Here the system is described as having local bonding between nearest neighbors, and the distortion is energetically stabilized by the overlap of partially filled degenerate molecular orbitals. When the number of bonding neighbors in the distorted structure is equal to the number of unoccupied states, only energetically lowered states are occupied. Fully occupied bonding and unoccupied antibonding orbitals are separated by an energy gap in the presence of the coordination-lowering distortion, leading to insulating behavior. This gap is equivalent to that derived from the Fermi surface driven sinusoidal distortion discussed above, since in both cases the distortion is stabilized by the lowering of occupied states.[9] Furthermore, the presence of defects in a CDW system can affect the distortion in a variety of ways. Ordering of atomic vacancies, requiring a supercell containing an integral number of vacancies, may be incompatible with the period of the Fermi surface nesting wave vector.

0163-1829/95/52(20)/14516(10)/$06.00

Additional well studied effects of doping include suppression of the CDW due to disorder[6] and tuning of the CDW wave vector through changes in the band filling.[7] Much attention has been paid to the effects of defects on CDW stability[10] and to the relationship between nonsinusoidal character and commensurability.[6,11] Neither the picture of a CDW as a Fermi surface driven instability of a metal nor the Jahn-Teller description allows the specific atomic displacements or consequences of defects to be predicted entirely from the nesting condition.

Understanding how the band structure drives distortions and accommodates defects requires a tunable system in which qualitatively different distortions are produced by continuous changes in electronic structure. In this paper we will show that the rare-earth polychalcogenides[12] RX_n (R denotes rare earth; X denotes S,Se,Te; n=2,2.5,3) are ideal for such experimental studies. Among the RX_n are members that variously host large commensurate distortions, ordered and disordered vacancy structures, and small-amplitude Fermi surface driven CDW's. These materials have the layered structure shown in Fig. 1, in which corrugated cubic rare-earth-chalcogen slabs alternate with planar chalcogen square lattices.[13] The RX_n have a remarkably simple electronic structure, as the bands associated with the rare earth-chalcogen slab atoms do not contribute to the Fermi surface, which is entirely derived from the square chalcogen sheets. Tight-binding band calculations for square chalcogen lattices reveal a simple Fermi surface geometry with substantial potential for nesting,[14] the essential features of which are supported by our experimental observations. This nesting can be tuned compositionally, as charge transfer from the rare earth determines the band filling in the chalcogen sheets. Varying the rare-earth from La to Tm in the RX_n compounds reduces the Te sheet lattice parameters[15] by 4% without changing the structure type or band filling.

The propensity for chalcogenides to host symmetry lowering distortions can be demonstrated with a simple chemical argument. Chalcogen atoms have two unoccupied states in degenerate p orbitals, and require two near neighbors in order to fill their valence shells through covalent bonding. The elemental chalcogens are subject to distortions that reduce coordination from sixfold, in the high-pressure phases, to twofold coordinated chains or rings at ambient pressure, where electrons are localized in fully occupied bonding orbitals.[16] Similarly, the square chalcogen sheets of the RX_n compounds may be expected to be subject to coordination-reducing distortions.[17] In fact, a rich variety of structural distortions are found in the RX_n compounds for different stoichiometries and chalcogens,[17] despite a simple but universal chalcogen sheet band structure. Commensurate CDW's have been observed in several rare-earth diselenides,[18] in which atomic displacements in the Se sheets lead to the formation of covalently bonded dimers. Similar distortions are observed in $R\mathrm{Se}_{1.9}$ compounds, where Se dimers and ordered vacancies make up the distorted Se sheet superstructure.[19] A site occupancy wave in partially occupied Se sheets has been proposed for a related material with a commensurate superlattice, $\mathrm{RbDy_3Se_8}$.[14,17] Yet another defective diselenide phase, $\mathrm{DySe}_{1.84}$, has an incommensurate superstructure that is close to one of the maximal Fermi surface nesting wave vectors calculated for a fully occupied Se sheet, with no evidence for vacancy ordering.[14]

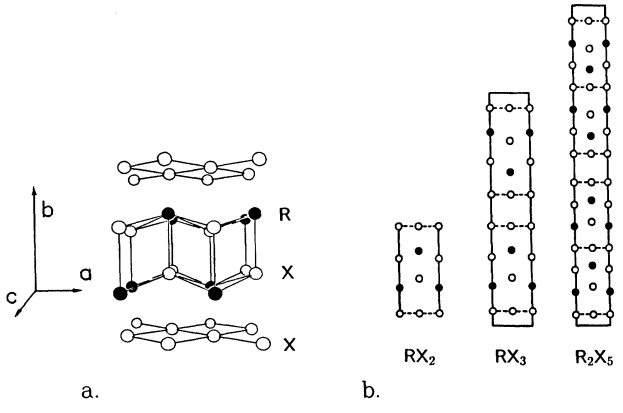

FIG. 1. (a) Basic Cu_2Sb component of the RX_n (n=2,2.5,3) crystal structure. Solid points are rare-earth atoms, open points chalcogen atoms. (b) The stoichiometric compounds RX_n (n=2,2.5,3) are differentiated by the number of double chalcogen layers present per unit cell, as shown in this view along the layer stacking direction.

Here we present evidence for a small-amplitude incommensurate CDW in a family of stoichiometric rare-earth polychalcogenides. Our previous single-crystal x-ray studies of $SmTe_3$ and Sm_2Te_5 revealed no evidence for CDW superstructure in the fully occupied Te sheets.[20] Electrical resistivity measurements revealed very large electrical anisotropies for these Sm polytellurides, but metallic behavior in both crystallographic directions for temperatures above 1.2 K.[20] However, these measurements do not rule out the presence of small-amplitude distortions that are stable above room temperature, and that only partially gap the Fermi surface.

In this paper we report the results of transmission electron microscopy on the rare-earth tritellurides. Through electron diffraction we have identified superlattice reflections in the Te sheets of tritellurides of La, Sm, Gd, Tb, Dy, Ho, Er, and Tm. We present a model for a small-amplitude periodic lattice distortion and show that the superlattice wave vector corresponds to Fermi surface nesting wave vectors determined from tight-binding band calculations. Under the chemical pressure obtained through rare-earth substitution the CDW remains stable, while the CDW wave vector remains close to the calculated nesting vector. Our results establish the rare-earth tritellurides as CDW hosts that can be described in terms of a small Fermi-surface-driven instability, with no evidence for substantial deviations from the sinusoidal CDW within the $R\mathrm{Te}_3$ system.

II. EXPERIMENTAL DETAILS

Single-crystal tritellurides of La, Sm, Gd, Tb, and Dy were prepared using a RbCl-LiCl flux method de-

scribed previously.[20] Ho and Er tritellurides were obtained using KI flux, as Rb was incorporated into the crystal structure for the heaviest rare earths. Because $TmTe_3$ has a melting point of 553 °C, lower than that of KI (680 °C), LiI flux was used to grow the Tm tritelluride. Very small RTe_3 crystals were also grown without flux, using the same temperature profiles as for the flux-grown samples. Electron microprobe analysis[21] was used to confirm the stoichiometry of crystals used for the transmission electron microscopy (TEM) experiments. These samples were cleaved with a razor blade, yielding electron transparent flakes that were mounted on amorphous carbon film on copper grids. Selected area diffraction patterns and bright- and dark-field images were obtained using a JEOL 2000FX transmission electron microscope equipped with a liquid-nitrogen stage, operating at 200 kV. Lattice constants were calibrated against those of a single-crystal Si TEM sample. Calculated diffraction patterns were obtained using the CERIUS^2 program.[22] The EHMACC software[23] was used for band-structure calculations.

III. EXPERIMENTAL RESULTS

Selected area diffraction patterns were obtained normal to the [010] zone axis in order to search for superlattice reflections corresponding to distortions from fourfold symmetry within the Te sheets. Figure 2(a) shows an experimental diffraction pattern for $SmTe_3$ at room temperature. The $(h0l)$ reciprocal lattice shown corresponds to the layer plane, with the beam parallel to the layer stacking direction ($\vec{b}$ axis), perpendicular to the foil-like sample. Intense diffraction spots are found for points with h and l even, appropriate to the space group $Cmcm$ previously assigned to the RTe_3 subcell.[13,20] These reflections are reproduced by a simulated diffraction pattern of the previously reported[13] $SmTe_3$ unit cell, as shown in Fig. 2(b). However, three additional groups of reflections are observed in the experimental patterns. While systematic extinctions are expected for $(h0l)$ points with h or l odd, we observe strong reflections where both h and l are odd, as well as weaker reflections for points with only one of h and l odd. In addition, pairs of satellite reflections, labeled $\pm\vec{q}$ in Fig. 2(a), are observed around reciprocal-lattice points. The intensities of these forbidden reflections are sample dependent, as Figs. 2(a), 2(c), and 2(d) illustrate. We will discuss each group of additional reflections separately. Ring patterns are also observed in some of the diffraction patterns. These rings indicate interplanar spacings corresponding to the structure of trigonal Te, and are most likely due to thin fine-grained polycrystalline films of unreacted Te on the surfaces of the samples.

We first consider the forbidden reflections on the reciprocal lattice. We find a strong correlation between defected sample morphology and the presence of the forbidden reflections. Stacking disorder was reported in the early x-ray studies of rare-earth polychalcogenide phases.[24] While stacking disorder along the $\vec{b}$ axis is not visible in our transmitted images of the $\vec{a}$-$\vec{c}$ plane, it will cause the reciprocal-lattice points to be elongated into rods in the [010] ($\vec{b}^*$) direction. Since the b lattice parameter is very large, the close proximity of the zero- and first-order Laue zones in the [010] direction causes the reciprocal-lattice rods from the first-order zone to project into the zero layer, yielding the forbidden reflections where both h and l are odd. The intensities of these reflections are increased when the sample is tilted, as illustrated by the convergent beam diffraction patterns shown in Fig. 3, taken in the $(h0l)$ plane for $SmTe_3$. In Fig. 3(a) the beam is converged on a spot a few nm in diameter and aligned along the [010] axis. Near the center of the pattern, the well-defined, intense disks satisfy h and l even. Out toward the higher-order Laue zone (HOLZ) ring, located near the edge of the pattern, disks from both zero- and first-order zones have comparable intensities, since here the reciprocal-lattice rods from both Laue zones intersect the Ewald sphere. Figure 3(b) shows that both zones are intercepted closer to the main beam if the sample is tilted away from the [010] axis. If the selected area patterns in Fig. 2 cover regions of the samples that are tilted relative to each other, intensities may then be expected for all points where $h+l$ is even. Such sample bending is evident in the transmitted images of the samples, as shown in Fig. 4. In this bright-field image of an $LaTe_3$ crystal, aligned close to the [010] axis, prominent bend contours are observed, both in highly defected and more uniform regions. We ascribe the appearance of reflections for reciprocal-lattice points with both h and l odd to the combined effects of stacking disorder and sample bending.

Reciprocal-lattice points with $h+l$ odd are extinct for all Laue zones in the subcell structure, but observed with weak intensity in our diffraction patterns, for samples grown with and without flux. Dark-field imaging in these points, shown in Fig. 5 for an $SmTe_3$ crystal aligned near [010], reveals small bright regions, suggesting that the weak reflections are due to small regions of material with a structure different from the reported RTe_3 subcell. Tilting the sample causes different small regions to be illuminated, indicating that small amounts of this second phase are distributed throughout the sample. R-Te phases reported in the literature[15] either have lattice parameters different from those of the RTe_3 sublattice, or are members of the RX_n family that share the extinction condition for $h+l$ odd. This suggests that the "second phase" may simply be regions of the RTe_3 crystal where the stacking is so corrupted as to eliminate the symmetry producing the systematic extinctions. Diffraction patterns taken on very uniform crystals, such as the region outlined with the rectangle in Fig. 4, yield much weaker reflections on forbidden reciprocal-lattice points, as demonstrated by the selected area diffraction pattern in Fig. 6. Here reciprocal-lattice points with $h+l$ odd are extremely weak, sometimes completely extinct. Points with both h and l odd, attributed to sample bending, are also very weak, while the satellites $\pm\vec{q}$ are quite intense. In summary, we find that the combination of stacking disorder and bent samples yields intensity on reciprocal-lattice points with both h and l odd, while forbidden reflections with one of h and l odd are produced by small

isolated patches in highly defected samples.

The satellite reflections $\pm\vec{q}$ have a different origin. Such satellites are present in $LaTe_3$ as well as in all existing tritellurides from Sm to Tm, and in samples grown with and without flux. The presence of the satellites indicates that an additional periodicity of wavelength $2\pi/|\vec{q}|$ is superimposed upon the undistorted cell, parallel to the $\vec{a}$ or $\vec{c}$ axes of the $R\mathrm{Te}_3$ subcell. The satellite reflections appear with the strongest intensities around reciprocal-lattice points where $h+l$ is odd. In nearly all samples the satellites appear in both the $\vec{a}^*$ and $\vec{c}^*$ directions, most often with two pairs of perpendicular satellites around the same point, as in Fig. 2(a). A few samples have satellites primarily in only one of the $\vec{a}^*$ or $\vec{c}^*$ directions, such as those in Fig. 2(c) and Fig. 6. The magnitude of $|\vec{q}|/|\vec{c}^*|$ is plotted in Fig. 7 for all rare-earth tritellurides studied. For $SmTe_3$ $|\vec{q}|/|\vec{c}^*|$ is close to (2/7), with no dependence on temperature detected between 90 and 273 K.

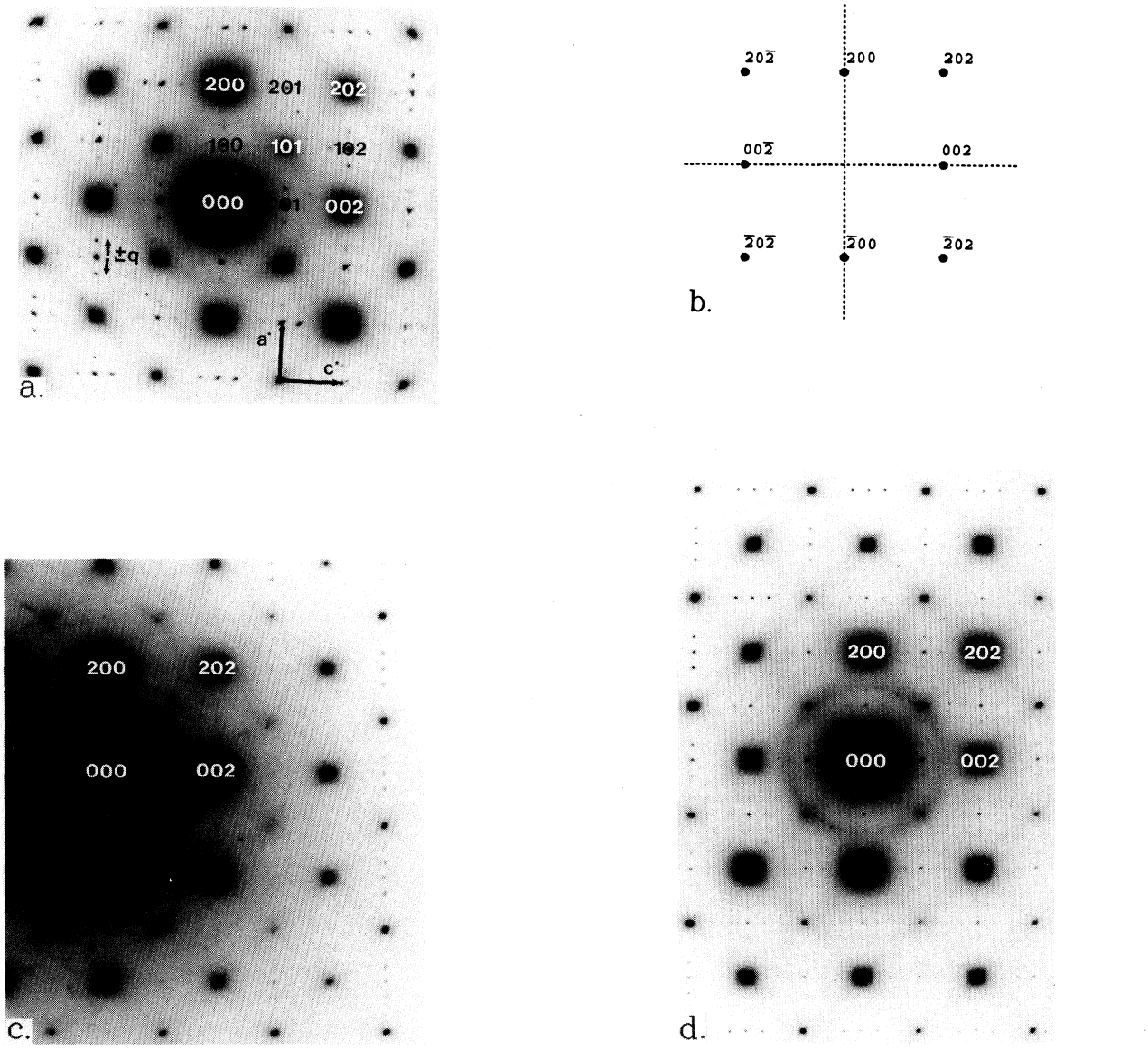

FIG. 2. Selected area diffraction patterns of rare-earth tritellurides in the $(h0l)$ plane. The central rings indicate the presence of disordered elemental Te, most likely due to thin polycrystalline films of unreacted Te on the crystal surfaces. (a) $SmTe_3$ crystal grown with RbCl/LiCl flux, at 273 K. The subcell reciprocal-lattice points are indexed, with satellite reflections labeled $\pm\vec{q}$. (b) Simulated pattern for undistorted $SmTe_3$ unit cell, with systematic extinctions for h or l odd. (c) $TmTe_3$ at 90 K. Sample grown with LiI flux. The appearance of ring patterns around peaks other than (000) is due to double diffraction. (d) $SmTe_3$ sample showing boxlike pattern of satellites, with vertical and horizontal satellites appearing in alternating rows.

The variation of $|\vec{q}|$ with rare earth will be addressed further below.

We ascribe the superlattice reflections to a periodic lattice distortion in the Te sheets. Since the form factor for high-order satellites falls off rapidly for small-amplitude structural distortions,[7,25] the lack of higher-order satellites in our experiment implies that the atoms

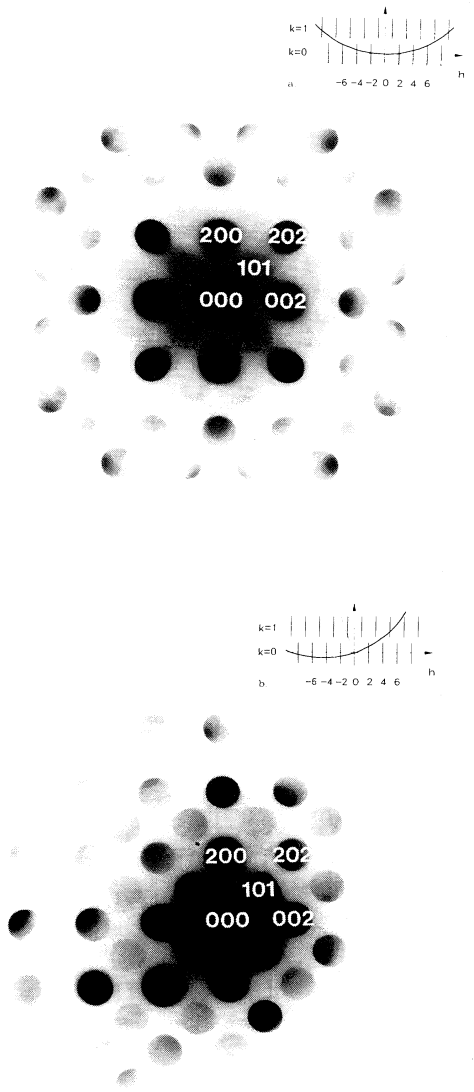

FIG. 3. (a) Convergent beam electron diffraction (CBED) pattern in $(h0l)$ plane for $SmTe_3$. Near the center of the pattern, disks satisfy h and l even, the expected subcell conditions. Points from the $k = 1$ Laue zone having h and l odd are intercepted for larger h and l. The inset illustrates the elongated diffraction rods in the h-k plane. The curved line (Ewald sphere construction) shows which reciprocal-lattice points are intercepted for beam aligned normal to the h-l plane. (b) CBED pattern on the sample in (a) tilted $\sim 20°$ away from the zone axis, as indicated in the inset. Near (000), disks from both $k = 0$ and $k = 1$ Laue zones have comparable intensities.

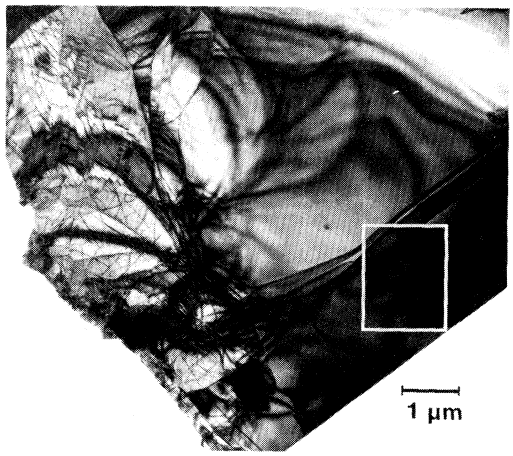

FIG. 4. Bright-field image of an $LaTe_3$ crystal, aligned near the [010] axis. Prominent bend contours are visible, both in the highly defected region on the left of the sample, and in the more uniform region on the right. The selected area diffraction pattern of Fig. 6 was taken in the area bounded by the rectangle at the lower right.

are only slightly displaced from the square-lattice positions. Our model, having a distortion within a 1×7 supercell, is shown in Fig. 8. Crosses in the figure indicate the square positions, while the circles show the new atom positions in the distorted phase. Here the displacements δx and δz in the $\vec{a}$ and $\vec{c}$ directions are proportional to $\sin(|\vec{q}|z)$, where z is the coordinate of the atom's undistorted position in the $\vec{c}$ direction in the supercell. This model yields the simulated diffraction pattern shown in Fig. 9(a) for a displacement amplitude of $3\%|\vec{c}|$. Second-order satellites, not observed experimentally, become visible in our simulations for distortion amplitudes exceeding 6%. Our observation that the satellites appear only

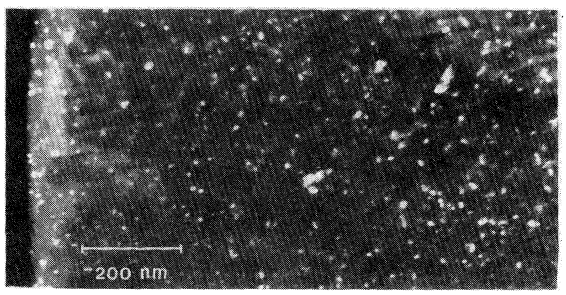

FIG. 5. Dark-field image of an $SmTe_3$ crystal taken in a forbidden reflection with $h + l$ odd. The sample is aligned near the [010] axis. The intensity comes from small patches on the sample, with different patches illuminated when the sample is tilted, suggesting that small regions have sufficient defects to reduce the crystal symmetry.

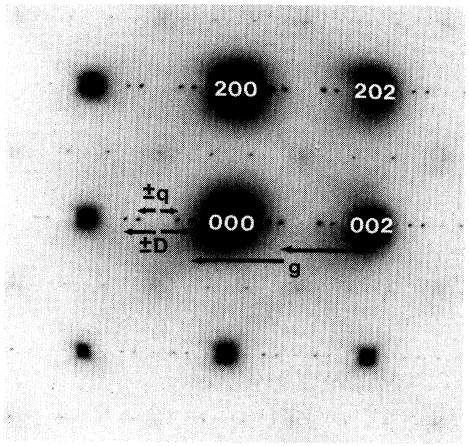

FIG. 6. Diffraction pattern in ($h0l$) plane taken in the region bounded by the rectangle in Fig. 4. Here the extinction conditions for h or l odd are nearly satisfied, while the subcell peaks (200-type) and satellites $\pm\vec{q}$ have strong intensities. Double diffraction through the wave vector $\vec{g} = \pm(\vec{c}^* + \vec{q})$ produces an additional set of spots, labeled $\pm\vec{D}$ in the figure.

around reciprocal-lattice points with $h + l$ odd requires that two phase angles be chosen relating the x and z displacements. In the model, δx and δz are 90° out of phase for each atom, so that all atoms are equidistant from their undistorted positions while their polar angles change continuously across the supercell. To reproduce the observation that the satellites appear predominantly around points with $h + l$ odd, the displacements of the atoms labeled 1 and 2, in the corner and center of the supercell, are 180° out of phase with each other. When this phase angle is intermediate between 90° and 180°, weak satellites appear around points where $h + l$ is even, an effect occasionally observed experimentally.

The model described above reproduces satellite reflections that appear in only one of the $\vec{a}^*$ or $\vec{c}^*$ directions. Two pairs of perpendicular satellites at each point can be produced either by perpendicularly oriented superlattice

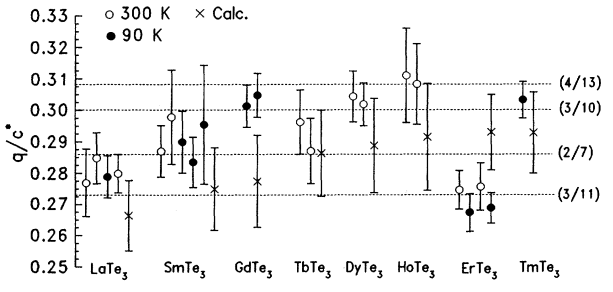

FIG. 7. Magnitudes of distortion wave vector observed in RTe$_3$ compounds. Open circles are room-temperature experiments; closed circles are measurements at 90 K. Crosses are calculated maximal Fermi surface nesting vectors as described in text.

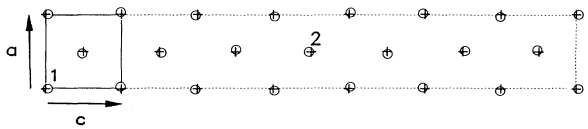

FIG. 8. Model Te sheet supercell with periodic lattice distortion. Square sheet positions are indicated by crosses, displaced atom positions by circles, as described in text. Atoms at the corner (1) and center (2) of the supercell are constrained to move in opposite directions, so that the displacements of atoms in the two rows are 180° out of phase with each other.

domains, or by alternating Te layers with distortion wave vector in the $\vec{a}^*$ and $\vec{c}^*$ directions. A simulated diffraction pattern corresponding to the latter situation is shown in Fig. 9(b). We ascribe the sample dependence of satellite orientations to different arrangements of distorted Te sheets relative to each other in the crystal. There remain several features observed occasionally in our diffraction patterns that we have not explained. We have not found an arrangement of distorted layers that can reproduce the intriguing boxlike pattern of satellites in Fig. 2(d). Mod-

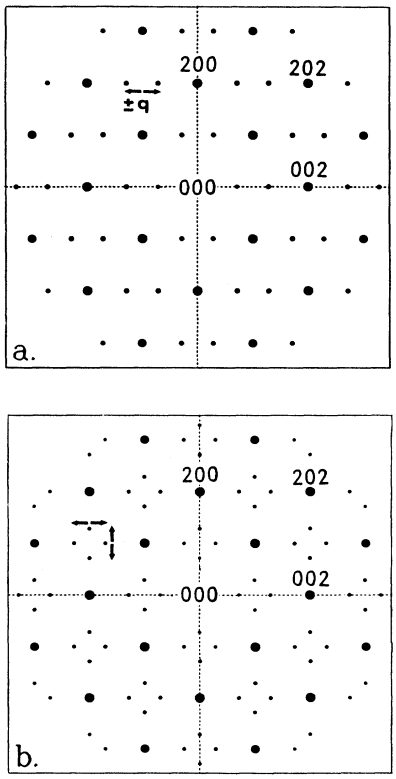

FIG. 9. Simulated ($h0l$) diffraction patterns. (a) Te supercell with model distortion shown in Fig. 5. (b) Supercell formed from a stack of two 7 × 7 layers with perpendicularly oriented distortions.

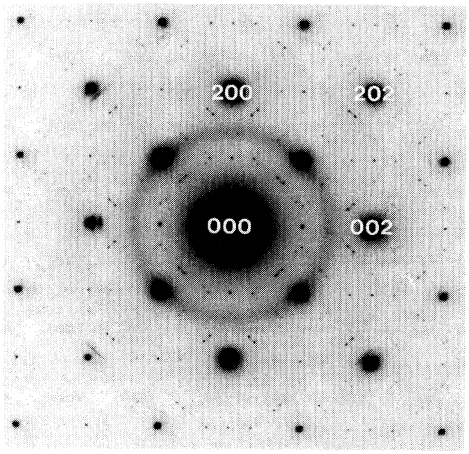

FIG. 10. Selected area diffraction pattern in $(h0l)$ plane for sample from an $SmTe_3$ batch in which the primary satellites at $(2/7)\vec{c}^*$ are accompanied by a more complicated pattern of satellites.

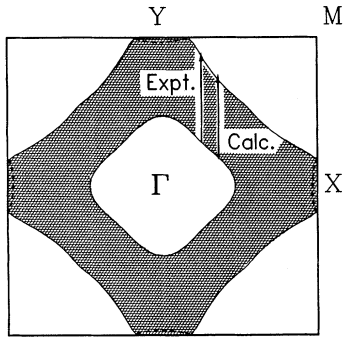

FIG. 11. Calculated Fermi surface for Te sheet with band filling appropriate to $SmTe_3$. Dashed and solid lines are Fermi surfaces for two separate bands, and the shaded region shows filled states. The observed distortion wave vector matches the calculated maximal nesting vector for the long parallel sheets of the Fermi surface. The size of the arrowheads indicates experimental and calculated error, shown as error bars in Fig. 7. Since the nesting sheets have some curvature, the calculated nesting vector was averaged over the region 0.10–$0.25\vec{a}^*$.

els incorporating stacked Te sheets that were rotated by 180° around either the a or b axis failed to yield satellites appearing around alternating rows of reciprocal-lattice points as observed in experiment. In the diffraction pattern of Fig. 6, additional spots $\pm\vec{D}$ are produced by double diffraction of the main (200-type) and satellite $(\pm\vec{q})$ spots, through the wave vector $\vec{g} = \vec{c}^* + \vec{q}$. For this double diffraction route, $|\vec{D}| = |\vec{c}^*| - 2|\vec{q}|$, and with $|\vec{q}|$ close to $(2/7)|\vec{c}^*|$, this yields $|\vec{D}| \approx (3/7)|\vec{c}^*|$, raising the question of whether the spots at $\pm\vec{D}$ may instead be higher-order superlattice peaks. However, we find that for samples where $|\vec{q}|/|\vec{c}^*|$ deviates from (2/7), such as $ErTe_3$, $\vec{q}$ and $\vec{D}$ are not commensurate within experimental error. In a few other samples, the satellites at $(2/7)\vec{c}^*$ are accompanied by a more complex pattern of satellites, shown in Fig. 10. Further work will be required to address these more complicated satellite patterns. In subsequent discussion we will only consider the primary satellites at $(2/7)\vec{c}^*$. Finally, we emphasize that the periodic lattice distortions discussed above are too small to lift the reciprocal-lattice extinctions, as demonstrated by our simulations, where systematic extinctions are maintained even in the presence of relatively intense satellites.

IV. DISCUSSION

We have identified structural distortions in the Te sheets of the rare-earth tritellurides. The superlattice wave vectors observed correspond very well to maximal Fermi surface nesting vectors determined from tight-binding band calculations. Figure 11 shows the quasi-two-dimensional Fermi surface calculated for a square Te sheet with lattice parameter corresponding to that of $SmTe_3$. The extended Hückel method[26] with conventional Te parameters was employed.[27] Band filling was determined by taking into account charge transfer from the rare earth, which previous magnetic susceptibility measurements found to be trivalent.[20] We assume that the rare-earth atom provides two electrons for bonding within the rare-earth-chalcogen slab, while the third electron is contributed to the sheet Te bands. Since there are two sheet Te atoms per rare earth, this leads to a band filling of 6.5 electrons per Te in the square sheet. Filled states are indicated by the shaded region, while solid and dashed lines show where two bands cross the Fermi level. This Fermi surface has long parallel sheets along the $(\vec{a}^* \pm \vec{c}^*)$ directions, which are nested by a wave vector that is the same as that observed experimentally within the errors of both experiment and calculation. This correspondence argues that the periodic lattice distortion in the Te sheets is driven by Fermi surface energetics, with a remarkably simple band structure dominated by sheet Te bands.

As Fig. 7 illustrates, CDW satellites are observed in the tritellurides across the rare-earth series, and we now consider the stability of the distortion. In the RTe_3 family, lattice constants decrease by 4% from $LaTe_3$ to $TmTe_3$, the rare-earth tritelluride with the smallest lattice constant. Calculated maximal nesting vectors for Te sheets with lattice constants appropriate to each rare earth are indicated with crosses on Fig. 7. The correspondence between the observed and calculated wave vector is retained across the series, with $|\vec{q}|/|\vec{c}^*|$ taking values between 0.27 and 0.31. Despite the proximity of $|\vec{q}|/|\vec{c}^*|$ to (2/7), which allows the distortion to be modeled in a 1×7 supercell, the CDW's of the RTe_3 when considered together are best described as incommensurate.

Since a Fermi surface driven CDW relies on having the energies of a large density of states at the Fermi level, $N(\varepsilon_F)$, lowered by the distortion,[1,4,6,7] the CDW is expected to be sensitive to experimental variation of $N(\varepsilon_F)$. In a simple metallic system, a decrease in cell volume is expected to broaden the bands and reduce $N(\varepsilon_F)$,[4] and so we would predict the CDW to be destabilized as

cell volume is reduced. This expectation is borne out by naive energy calculations. Figure 12(a) shows the results of second moment scaled[28] Hückel calculations for distorted Te supercells with varying CDW amplitudes. Here the band energies for the distorted structures have been calculated for each lattice constant, and referenced to the energy of a square lattice of the same cell size. For each CDW amplitude, the distortion is increasingly stable at larger cell volume. The calculations also predict that larger-amplitude distortions are more quickly destabilized with pressure, as illustrated in Fig. 12(b), which shows the critical lattice constant for CDW destabilization as a function of distortion amplitude. As we observed CDW satellites in $TmTe_3$, we can estimate from the energy calculations that the CDW amplitude in the rare-earth tritellurides is less than $6\%|\vec{c}|$, consistent with the absence of higher-order satellite reflections. We caution that this technique only provides an upper bound on the CDW amplitude, as the second-moment scaled Hückel method is known to underestimate the energetic cost of increased CDW amplitudes for rare-earth polyselenides.[17]

It is instructive to compare the incommensurate Fermi surface nesting CDW's of the $R\mathrm{Te}_3$ with the large commensurate distortion of $LaSe_2$, which has previously been approached from the point of view of a Jahn-Teller instability.[17] In the Se sheets of $LaSe_2$, the bonding orbitals of covalent Se dimers are exactly filled by the number of electrons available in the system. While a localized Jahn-Teller description would consequently be adequate for $LaSe_2$, it would be problematic for the metallic $R\mathrm{Te}_3$. Here, the rare-earth contributes an odd number of electrons per unit cell to the Te sheets. Since each chalcogen atom or chain requires two electrons to fill its empty s/p states, the electronic requirements of covalently bonded chalcogen chains cannot be satisfied in the tritellurides. This makes the $R\mathrm{Te}_3$ distortions impossible to interpret in a literal Jahn-Teller picture, and emphasizes the need for a more general CDW description that encompasses the entire family of distortions observed in chalcogen square lattices.

The similarity between the $LaSe_2$ and $R\mathrm{Te}_3$ systems is apparent, however, from a comparison of their calculated Fermi surfaces. The primary difference between the Fermi surfaces of the di- and trichalcogenides is due to their respective band filling, as illustrated in Fig. 13. The RX_2 stoichiometry has one rare-earth per sheet chalcogen atom, leading to a band filling of $7e$/chalcogen, larger than the $6.5e$/chalc. of the RX_3 compounds. Figure 13(a) shows the calculated Fermi surface of the Se sheet of $LaSe_2$. The wave vector $\vec{q} = (1/2)\vec{a}^*$, corresponding to the experimentally observed cell doubling,[18] nests sheets of the Fermi surface near the edge of the Brillouin zone. The calculated Fermi surface of a square Te lattice with the same band filling, shown in Fig. 13(b), corresponds to $LaTe_2$ and is nearly identical to the $LaSe_2$ Fermi surface. As band filling in the Te sheet is reduced towards that of the $R\mathrm{Te}_3$ compounds ($6.5e$/Te), as shown in Figs. 13(c) and 13(d), the nesting sheets near the zone edge are continuously degraded. Near the $R\mathrm{Te}_3$ band filling nesting across the sheets forming in the $(\vec{a}^* \pm \vec{c}^*)$ directions becomes more favorable. These calculations emphasize the equivalent origins of the distortions in dimerized diselenides and metallic tritellurides. Finally, we observe that the rare-earth polytellurides are an especially appropriate experimental family for further study of CDW's in chalcogen square lattices. While the rare-earth dichalcogenides are obtainable for both Se and Te, the lower band filling of the stoichiometries R_2X_5 and RX_3 are found only for polytellurides. A further

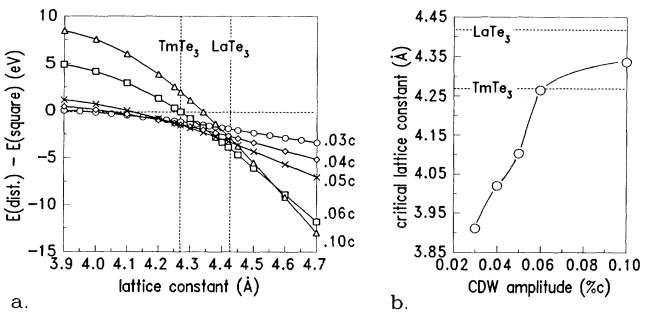

FIG. 12. (a) Calculated band energies for distorted Te supercells referenced to the energy of the undistorted square lattice, as a function of lattice constant. The different curves correspond to CDW's of different amplitudes, and show that larger distortions are increasingly stable for larger cell volume. (b) Critical lattice constant for CDW destabilization as a function of distortion amplitude. In both figures, dashed lines show extremal $R\mathrm{Te}_3$ lattice parameters, and solid lines are guides for the eye.

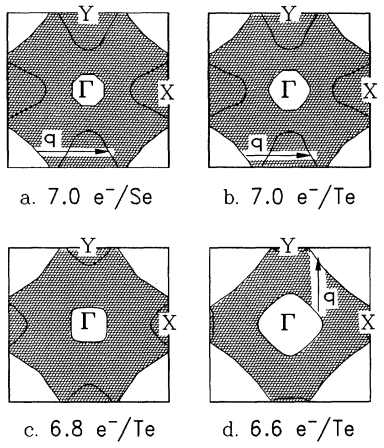

FIG. 13. (a) Calculated Fermi surface for Se sheet with band filling of 7.0 electrons/sheet Se atom, appropriate for $LaSe_2$. The nesting vector $\vec{q} = \vec{a}^*/2$ corresponds to the experimentally observed cell doubling of this compound. (b) The Fermi surface of a square Te sheet with the same band filling ($7.0e$/Te) is virtually identical to the $LaSe_2$ surface. Reducing the band filling towards the $6.5e$/Te of the $R\mathrm{Te}_3$ compounds, (c) and (d), degrades the nesting near the zone edge in favor of that across the parallel sheets in the $(\vec{a}^* \pm \vec{c}^*)$ directions.

advantage of the tritellurides is the simplicity of their fully occupied double Te sheets. Previous single-crystal x-ray studies[20,29] found that the single Te layers of $SmTe_2$ and Sm_2Te_5 have vacancies, which would be expected to complicate the energetics of the CDW. Our observations establish the rare-earth polychalcogenides as CDW hosts in which a variety of structural distortions result from a very simple band structure, which can be tuned experimentally and compositionally within the RX_n family.

V. SUMMARY

The layered rare-earth polychalcogenides are a charge-density wave (CDW) family hosting a variety of structural distortions in their quasi-two-dimensional square chalcogen sheets. Through transmission electron microscopy we have studied the structure and morphology of the rare-earth tritellurides. From electron diffraction we identified superlattice reflections indicating the presence of incommensurate distortions in the layer plane, which we model with sinusoidal atomic displacements in the square Te sheets of these compounds. The observed superlattice wave vector corresponds to the maximal Fermi surface nesting wave vector determined from extended Hückel tight-binding band calculations. The CDW is stable under the volume decrease obtained by substituting the heavier rare earths, while energy calculations suggest that large-amplitude distortions are suppressed under this chemical pressure. Our results indicate that the rare-earth tritellurides host small-amplitude Fermi surface driven distortions. The experimental observations are compatible with sinusoidal atomic displacements, in contrast to the large commensurate distortions and ordered vacancy structures found in other rare earth polychalcogenide phases. Our observations establish the rare-earth polychalcogenides as a model CDW family, in which incommensurate small-amplitude CDW's, large Jahn-Teller-like distortions, and ordered vacancy structures all result from a very simple but universal chalcogen sheet band structure.

ACKNOWLEDGMENTS

Acknowledgment is made to the donors of The Petroleum Research Fund, administered by the American Chemical Society, for partial support of this research. We thank the A. P. Sloan Foundation and the J. D. and C. T. MacArthur Foundations for fellowships granted to S.L. This research was supported by the National Science Foundation under Grant No. DMR-9319196.

[1] F. J. DiSalvo, in *Electron-Phonon Interactions and Phase Transitions*, edited by T. Riste (Plenum, New York, 1977).
[2] For reviews, see *Electronic Properties of Inorganic Quasi-One-Dimensional Compounds*, edited by P. Monceau (Reidel, Dordrecht, 1985); *Crystal Chemistry and Properties of Materials with Quasi-One-Dimensional Structures*, edited by J. Rouxel (Reidel, Dordrecht, 1986).
[3] E. Canadell and M.-H. Whangbo, Chem. Rev. **91**, 965 (1991).
[4] R. H. Friend and D. Jérome, J. Phys. C **12**, 1441 (1979), and references therein.
[5] Y. Shimoi and H. Fukutome, Prog. Theor. Phys. **87**, 307 (1992).
[6] R. L. Withers and J. A. Wilson, J. Phys. C **19**, 4809 (1986).
[7] J. A. Wilson, F. J. DiSalvo, and S. Mahajan, Adv. Phys. **24**, 117 (1975).
[8] T. A. Albright, J. K. Burdett, and M.-H. Whangbo, *Orbital Interactions in Chemistry* (Wiley, New York, 1985).
[9] M.-H. Whangbo and E. Canadell, J. Am. Chem. Soc. **114**, 9587 (1992).
[10] R. M. Fleming, S. A. Sunshine, C. H. Chen, L. F. Schneemeyer, and J. V. Waszczak, Phys. Rev. B **42**, 4954 (1990), and references therein.
[11] W. L. McMillan, Phys. Rev. B **14**, 1496 (1976).
[12] E. Bucher, K. Andres, F. J. DiSalvo, J. P. Maita, A. C. Gossard, A. S. Cooper, and G. W. Hull, Jr., Phys. Rev. B **11**, 500 (1975), and references therein.
[13] B. K. Norling and H. Steinfink, Inorg. Chem. **5**, 1488 (1966); M.-P. Pardo and J. Flahaut, Bull. Soc. Chim. **10**, 3658 (1967); R. Wang, H. Steinfink, and W. F. Bradley, Inorg. Chem. **5**, 142 (1966).
[14] B. Foran, S. Lee, and M. C. Aronson, Chem. Mater. **5**, 974 (1993).
[15] P. Villars and L. D. Calvert, *Pearson's Handbook of Crystallographic Data for Intermetallic Phases* (American Society for Metals, Metals Park, OH, 1991).
[16] R. M. Martin, G. Lucovsky, and K. Helliwell, Phys. Rev. B **13**, 1383 (1976).
[17] S. Lee and B. Foran, J. Am. Chem. Soc. **116**, 154 (1994).
[18] J.-P. Marcon and R. Pascard, C. R. Acad. Sci. Paris **266**, 270 (1968); S. Bénazeth, D. Carré, and P. Laruelle, Acta. Crystallogr. Sec. B **38**, 33 (1982).
[19] M. Grupe and W. Urland, J. Less-Common Met. **170**, 271 (1991); P. Plambeck-Fischer, W. Abriel, and W. Urland, J. Solid State Chem. **78**, 164 (1989).
[20] E. DiMasi, B. Foran, M. C. Aronson, and S. Lee, Chem. Mater. **6**, 1867 (1994).
[21] Cameca MBX automated microprobe WDS system with elemental tellurium and rare-earth phosphates as standards. Supported by NSF Grant No. EAR-82-12764.
[22] CERIUS^2 Chemical Simulations Software Package, Molecular Simulation Inc., Burlington MA, 1994.
[23] M.-H. Whangbo, M. Evain, T. Hughbanks, M. Kertesz, S. Wijeyesekera, C. Wilker, C. Zheng, and R. Hoffmann, EHMACC program for extended Hückel molecular and crystal calculations.
[24] T. H. Ramsey, H. Steinfink, and E. J. Weiss, Inorg. Chem. **4**, 1154 (1965).
[25] A. W. Overhauser, Phys. Rev. B **3**, 3173 (1971).
[26] R. Hoffmann, J. Chem. Phys. **39**, 1397 (1963); M.-H.

Whangbo, R. Hoffmann, and R. B. Woodward, Proc. R. Soc. London Ser. A **366**, 23 (1979).

[27] We used 170 k points per octant of the Brillouin zone, with Te parameters from E. Canadell, Y. Mathey, and M.-H. Whangbo, J. Am. Chem. Soc. **110**, 104 (1988).

[28] S. Lee, J. Am. Chem. Soc. **113**, 8611 (1991); Acc. Chem. Res. **24**, 249 (1991).

[29] E. DiMasi, M. C. Aronson, B. Foran, and S. Lee, Physica B (Amsterdam) **206&207**, 386 (1995).

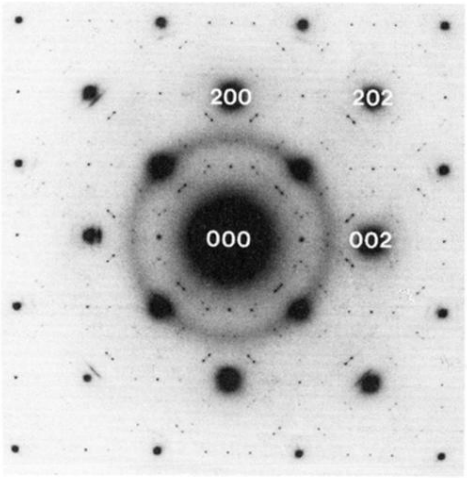

FIG. 10. Selected area diffraction pattern in $(h0l)$ plane for sample from an $SmTe_3$ batch in which the primary satellites at $(2/7)\vec{c}^*$ are accompanied by a more complicated pattern of satellites.

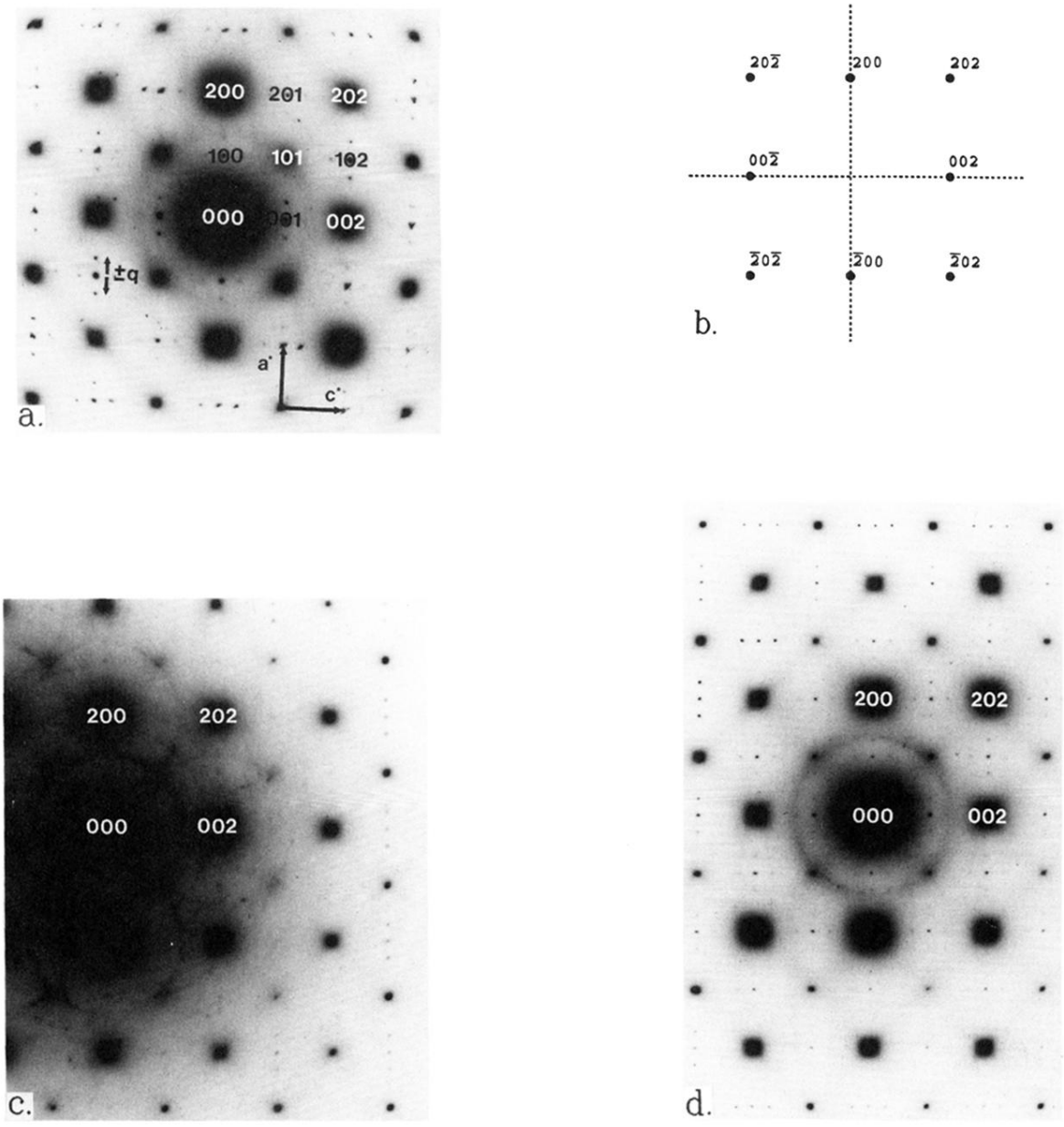

FIG. 2. Selected area diffraction patterns of rare-earth tritellurides in the $(h0l)$ plane. The central rings indicate the presence of disordered elemental Te, most likely due to thin polycrystalline films of unreacted Te on the crystal surfaces. (a) $SmTe_3$ crystal grown with RbCl/LiCl flux, at 273 K. The subcell reciprocal-lattice points are indexed, with satellite reflections labeled $\pm\vec{q}$. (b) Simulated pattern for undistorted $SmTe_3$ unit cell, with systematic extinctions for h or l odd. (c) $TmTe_3$ at 90 K. Sample grown with LiI flux. The appearance of ring patterns around peaks other than (000) is due to double diffraction. (d) $SmTe_3$ sample showing boxlike pattern of satellites, with vertical and horizontal satellites appearing in alternating rows.

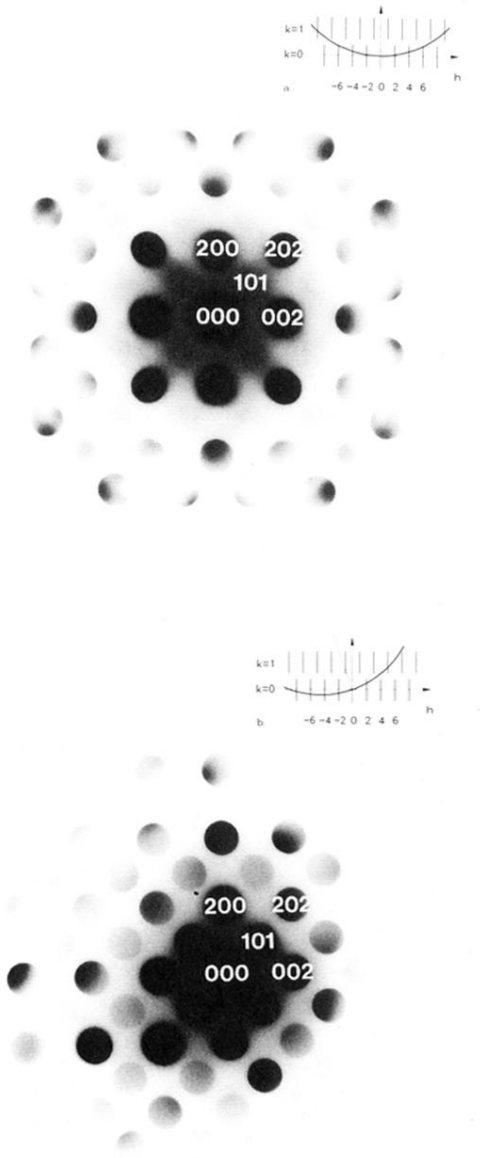

FIG. 3. (a) Convergent beam electron diffraction (CBED) pattern in ($h0l$) plane for $SmTe_3$. Near the center of the pattern, disks satisfy h and l even, the expected subcell conditions. Points from the $k = 1$ Laue zone having h and l odd are intercepted for larger h and l. The inset illustrates the elongated diffraction rods in the h-k plane. The curved line (Ewald sphere construction) shows which reciprocal-lattice points are intercepted for beam aligned normal to the h-l plane. (b) CBED pattern on the sample in (a) tilted $\sim 20°$ away from the zone axis, as indicated in the inset. Near (000), disks from both $k = 0$ and $k = 1$ Laue zones have comparable intensities.

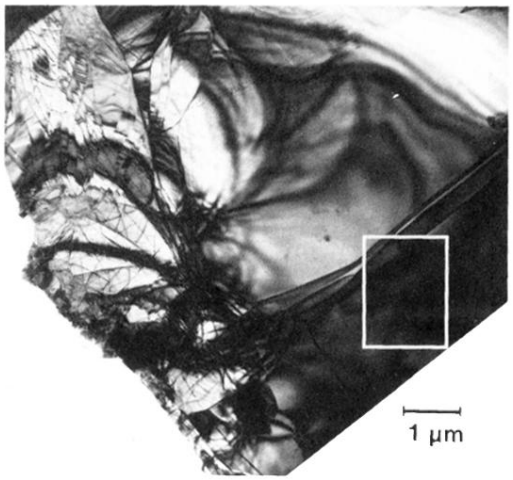

FIG. 4. Bright-field image of an $LaTe_3$ crystal, aligned near the [010] axis. Prominent bend contours are visible, both in the highly defected region on the left of the sample, and in the more uniform region on the right. The selected area diffraction pattern of Fig. 6 was taken in the area bounded by the rectangle at the lower right.

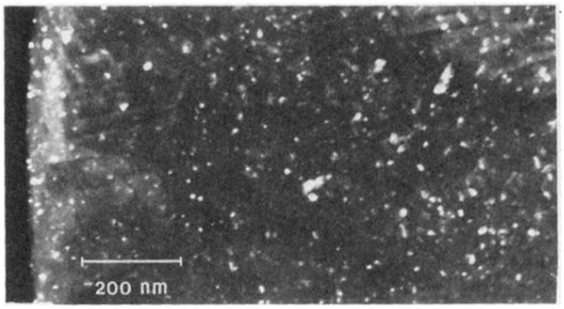

FIG. 5. Dark-field image of an $SmTe_3$ crystal taken in a forbidden reflection with $h + l$ odd. The sample is aligned near the [010] axis. The intensity comes from small patches on the sample, with different patches illuminated when the sample is tilted, suggesting that small regions have sufficient defects to reduce the crystal symmetry.

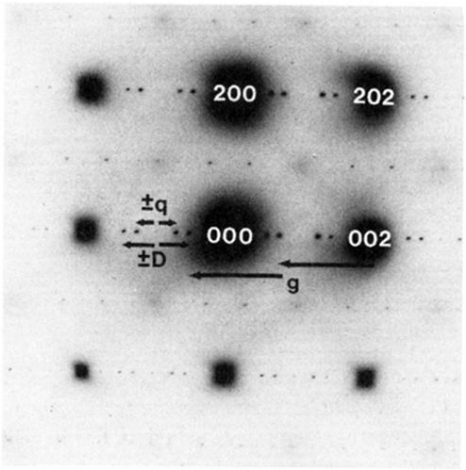

FIG. 6. Diffraction pattern in $(h0l)$ plane taken in the region bounded by the rectangle in Fig. 4. Here the extinction conditions for h or l odd are nearly satisfied, while the subcell peaks (200-type) and satellites $\pm\vec{q}$ have strong intensities. Double diffraction through the wave vector $\vec{g} = \pm(\vec{c}^* + \vec{q})$ produces an additional set of spots, labeled $\pm\vec{D}$ in the figure.